Journal of Magnetic Resonance 211 (2011) 80–88

Contents lists available at ScienceDirect

Journal of Magnetic Resonance

journal homepage: www.elsevier.com/locate/jmr

Linear Response Equilibrium versus echo-planar encoding for fast high-spatial resolution 3D chemical shift imaging

Rudolf Fritz Fischer [a], Christof Baltes [a], Kilian Weiss [a], Aju Pazhenkottil [b], Markus Rudin [a], Peter Boesiger [a], Sebastian Kozerke [a,*]

[a] Institute for Biomedical Engineering, University and ETH Zurich, Gloriastrasse 35, CH-8092 Zurich, Switzerland
[b] Cardiac Imaging, University Hospital Zurich, Rämistrasse 100, CH-8091 Zurich, Switzerland

ARTICLE INFO

Article history:
Received 22 November 2010
Revised 19 March 2011
Available online 3 May 2011

Keywords:
Spectroscopic imaging
Linear Response Equilibrium
Echo-planar spectroscopic imaging
Signal-to-noise ratio
Atherosclerotic plaque

ABSTRACT

In this work Linear Response Equilibrium (LRE) and Echo-planar spectroscopic imaging (EPSI) are compared in terms of sensitivity per unit time and power deposition. In addition an extended dual repetition time scheme to generate broad stopbands for improved inherent water suppression in LRE is presented. The feasibility of LRE and EPSI for assessing cholesterol esters in human carotid plaques with high spatial resolution of $1.95 \times 1.15 \times 1.15\ mm^3$ on a clinical 3T MR system is demonstrated.

In simulations and phantom experiments it is shown that LRE has comparable but lower sensitivity per unit time relative to EPSI despite stronger signal generated. This relates to the lower sampling efficiency in LRE relative to EPSI as a result of limited gradient performance on clinical MR systems. At the same time, power deposition of LRE is significantly reduced compared to EPSI making it an interesting niche application for in vivo high field spectroscopic imaging of metabolites within a limited bandwidth.

1. Introduction

In vivo applications of chemical shift imaging (CSI) [1] are often limited by long total scan durations. Many approaches of fast spectroscopic imaging methods (SI) have thus been proposed to significantly reduce the total measurement time.

Besides the use of rapid pulse sequences, often derived from fast imaging methods, parallel imaging [2], fractional *k*-space sampling [3] and non-Cartesian *k*-space trajectories [4,5] have been demonstrated to achieve reductions in total measurement time.

It has been shown that simultaneous encoding of spatial and spectral information does not change sensitivity per unit time (SNR_t) as long as the total acquisition window is kept constant [6]. In many fast spectroscopic imaging techniques gradients for frequency encoding are applied during readout. Accordingly, the total measurement time is divided by the number of spatial points encoded within the acquisition window.

Steady-state free precession sequences (SSFP) offer a high signal-to-noise ratio within short scan times and are therefore interesting for fast spectroscopic imaging. Non-balanced [7,8] as well as fully balanced sequences [9] have been designed for spectroscopic imaging purposes. The application of balanced SSFP in particular has been of great interest as it provides the highest sensitivity per unit time of all imaging sequences [10].

The Linear Response Equilibrium (LRE) scheme is based on a steady-state free precession sequence with small flip angles and fully balanced gradients [11]. Herein, the signal is acquired during the steady-state of a periodically evolving spin system. In contrast to the common balanced SSFP scheme employing relatively large flip angles, there is no formation of an echo between two subsequent pulses. Instead, a longer time span of nearly free precession, referred to as T_s, comprising multiple equidistant pulses is exploited before the signal is refocused back to the initial state. During this period T_s of nearly free precession chemical shift and spatial information is encoded by repetitively traversing one or multiple *k*-space lines on a Cartesian grid. The train of excitation pulses within T_s results in a periodic pattern of pass- and stopbands in the frequency domain with a periodicity given by the inverse of the repetition time T_R. By modulating the excitation angles within one period, the spectral response of LRE is shaped to specifically excite spectral regions of interest. In turn, the periodic excitation pattern generated allows for intrinsic water suppression by centering a stopband region at the water resonance.

Echo-planar spectroscopic imaging (EPSI) [12,13] has been well established as it provides spatial-spectral encoding that has, gradient ramp sampling provided, the same SNR_t as CSI [6]. It has been applied to human brain [13], breast [14] and calf muscle [15], as well as to tumor characterization in rodents [16,17] and murine prostate [18].

* Corresponding author. Fax: +41 44 632 1193.
E-mail addresses: fischer@biomed.ee.ethz.ch (R.F. Fischer), cbaltes07@gmail.com (C. Baltes), kweiss@biomed.ee.ethz.ch (K. Weiss), Aju.Pazhenkottil@usz.ch (A. Pazhenkottil), rudin@biomed.ee.ethz.ch (M. Rudin), boesiger@biomed.ee.ethz.ch (P. Boesiger), kozerke@biomed.ee.ethz.ch (S. Kozerke).

1090-7807/$ - see front matter © 2011 Elsevier Inc. All rights reserved.
doi:10.1016/j.jmr.2011.04.006

Lipids in atherosclerotic lesions are supposed to be a key factor for the stability of atherosclerotic plaques and a marker for the risk of thrombotic events and embolism [19]. A particularly interesting potential application of fast spectroscopic imaging methods relates to the characterization of vascular plaques providing information that goes beyond the usual contrasts generated with MR imaging methods. Multi-contrast weighted MRI has become a standard tool for distinguishing different plaque components with a high specificity reported [20]. Nevertheless, several authors have emphasized problems in the unique differentiation of plaque components [21] and concerns regarding the identification of the lipid rich necrotic core have been raised [22]. To this end, single voxel spectroscopy has been used to collect lipid spectra of atherosclerotic plaque samples at body temperature ex vivo [23–25] allowing for unambiguous quantification of liquid cholesterol esters, a major content of human atheroma [26]. The problem of poor spatial information and contamination of spectra by inaccurate voxel placement has been addressed by image guided spectroscopy [27] and projection-reconstruction techniques [28]. Spectroscopic imaging, on the other hand, promises precise localization of lipid depositions as well as information on spatial variations of plaque composition. This application is, however, very challenging as reliable quantification demands high spatial and spectral resolution within reasonable scan times.

The objectives of the present work were to compare sensitivity per unit time, resolution limits and power deposition of both LRE and EPSI using computer simulations and phantom experiments. A modification to LRE employing alternating repetition times is proposed to extend the stopband width limited by T_R constraints at clinical MR systems. Finally, ex vivo lipid spectra of human atherosclerotic plaque are demonstrated revealing local differences in abundance and composition of lipid cores.

2. Methods

2.1. Theory

2.1.1. Linear Response Equilibrium

In LRE the steady-state signal is generated by a train of small hard radiofrequency (RF) pulses with periodically alternating flip angles (Fig. 1). Based on a small tip angle approach, a desired excitation profile in the frequency domain can be designed by modulating the RF-amplitudes [11]. In the following the envelope function of the flip angles will be referred to as *flip function* and the steady-state response in the frequency domain will be called *excitation function*.

According to [11] the steady-state signal is a sum of Lorentzian peaks weighted by the Fourier coefficients $\tilde{\alpha}_n$ of the flip function $\alpha(t)$ and the transverse magnetization M_{xy} can be written as:

$$M_{xy}(t,\Delta\omega) \approx \sum_{n=-\infty}^{\infty} C_{\Omega_n} e^{i\Omega_n t}, \tag{1}$$

with

$$C_{\Omega_n} = M_0 \sum_{k=-\infty}^{\infty} \tilde{\alpha}_{n-kN} \frac{i/T_2 + (\Omega_n - \Delta\omega)}{1/T_2^2 + (\Omega_n - \Delta\omega)^2}.$$

Here, M_0 is the equilibrium magnetization, $\Delta\omega$ is the off-resonance frequency and $\{\Omega_n = 2\pi n/T_S\}_{n\in z}$ is the set of discrete excited frequencies that is defined by $T_S = N \cdot T_R$, the period of $\alpha(t)$. Though RF-pulses are applied every T_R expression (1) describes a state of coherent spins having approximately the same phase evolution as in free precession over a time span of *multiple* T_R making the steady-state suited for spectroscopy. T_S determines the duration of the spectral readout.

For simplicity we use flip functions $\alpha(t)$ of the type

$$\alpha(t) = \alpha_0 \sum_{j=-m}^{m} \cos(\Omega_j t), \quad m \leqslant (N-1)/2, \tag{2}$$

exciting a passband formed by a subset of $(2m+1) \leqslant N$ coherent frequencies $\{\Omega_j\}_{j\in\{-m,\ldots,m\}}$ with constant amplitude α_0 (Fig. 2).

Based on a second order perturbation approach expression (1) has been shown to hold for designing an excitation pattern of pass- and stopbands by an appropriate choice of $\alpha(t)$ [11]. Nevertheless, higher order terms have to be considered when calculating spectral peak amplitudes and the influence of relaxation time constants. Accordingly, for simulation purposes, the forward Bloch equations were solved numerically using a matrix description of pulses and inter pulse periods of free precession with full relaxation terms [29].

Steady-state solutions are used to estimate signal-to-noise ratios. Sensitivity is calculated from the spectral amplitude S the standard deviation of the spectral noise σ_{spec} and the total measurement time:

$$\mathrm{SNR}_t = \frac{S}{\sqrt{T_{meas}}\sigma_{spec}}. \tag{3}$$

In view of in vivo applications of spectroscopic imaging techniques at high field strength, specific absorption rates (SAR) are an issue. This is of particular relevance for sequences with short T_R [30], such as LRE. While relatively large flip angles are used in conventional balanced SSFP type sequences, LRE incorporates

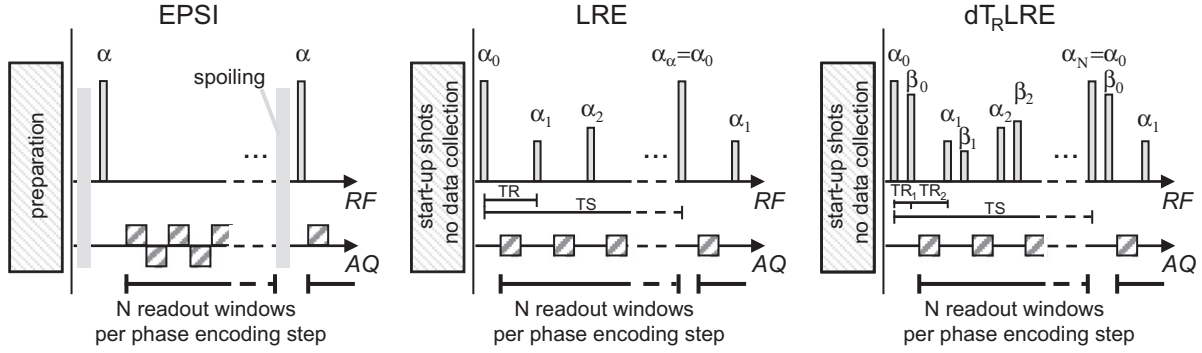

Fig. 1. Pulse sequence diagrams of EPSI, LRE and dT_RLRE. EPSI: chain of N frequency encoded acquisition windows after each excitation pulse and phase encoding step. k-Space read out direction alternates between neighboring echoes due to zigzag readout gradients. Residual transverse magnetization is spoiled before the next excitation. LRE: pulse amplitudes, given by Fourier analysis of the desired response in frequency space, vary with period N. Data acquisition in steady-state with totally balanced gradients after a number of start-up shots. For each phase encoding step spectrally resolved signal is acquired by reading out frequency encoded steady-state signal in N readout windows at different time points of the periodic signal evolution. dT_RLRE: sequence scheme with alternating T_R. Signal is read out only within T_{R2}. The second series of pulses β_i, also with period N, is used for shaping the frequency response and generating larger stopbands.

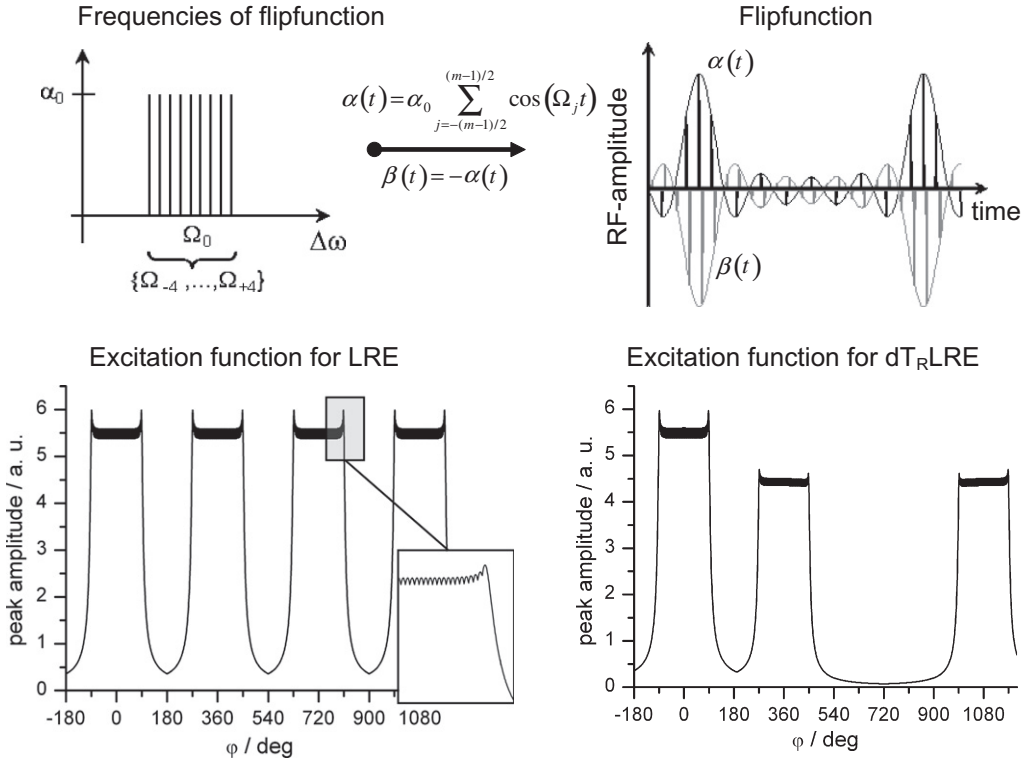

Fig. 2. Coherent set of discrete frequencies selected for excitation with constant amplitude α_0 (upper left panel). Resulting flip functions $\alpha(t)$ and $\beta(t)$ that determine the RF-amplitudes at time points $j\cdot T_{R1}$ and $jT_{R2}, j\in\mathbb{N}$ respectively (black and grey bars; upper right panel). β is only used for dT_RLRE. The lower row shows simulated peak amplitudes for common LRE and dT_RLRE respectively. A broad, deep stopband appears in the excitation function of dT_RLRE. The inset illustrates an enlarged section of the LRE passband revealing moderate ripples. Simulation parameters: T_R = 3.2ms; T_S = 496ms; Δf = 2 Hz; T_1 = 500 ms, T_2^* = 45 ms; flip function parameters: N = 155; $(2m+1)$ = 79; $\alpha_0 = 0.3°$ and $\alpha_0=\beta_0=0.15°$ for LRE and dT_RLRE, respectively (see Eqs. (2) and (8)).

small flip angles into the flip function. The energy density w of an RF-waveform with magnetic induction $B_1(t)$ and duration τ quantifies the relative power consumption:

$$w\propto\int_0^\tau B_1(t)B_1^*(t)dt. \tag{4}$$

Assuming arbitrary but identical RF-shapes and given $w\propto|B_1|^2\propto\alpha^2$ the average total quadratic flip angle per time unit is a measure for the power deposition. For flip functions according to Eq. (2) with N pulses per T_s it can be shown that the average quadratic flip angle is given by (Appendix):

$$w\propto\left\langle\alpha(t)^2\right\rangle=\frac{1}{T_S}\sum_{k=0}^{N-1}\alpha(k\cdot T_R)^2=\frac{(2m+1)|\alpha_0|^2}{T_R}. \tag{5}$$

Since $\alpha_0\cdot(2m+1)=\alpha(t=0)$ corresponds to the maximum flip angle in the flip function, the total power deposition per time unit is thus proportional to the product of the maximum flip angle and the amplitude α_0.

2.1.2. Dual-T_R Linear Response Equilibrium

A theoretical framework for an extension of LRE employing an alternating repetition time is given herein. In analogy to imaging sequences with varying T_R [31–34] the new sequence aims at increasing water suppression.

The spectral bandwidth Δf in LRE is limited by the minimum T_R achievable. On modern MR systems repetition times on the order of 2 ms can be achieved corresponding to a maximum bandwidth of $\Delta f\approx 500$ Hz. At 3 T this bandwidth may, however, not be sufficient to cover the range of resonances present.

Several variants of steady-state free precession sequences for MR imaging have been developed to shape the excitation function and to suppress frequency ranges in the steady-state response. Modulations of pulse phases [35] or flip angles [11,29,36] allow for tailoring of passbands and stopbands. However, the width of suppressed and excited regions in LRE remains limited by the $1/T_R$-periodicity of the flip function according to the formal solution of the Bloch equations (see Appendix).

To overcome the $1/T_R$ periodicity of the excitation function alternating T_R's may be used following up on previous work concerning balanced SSFP sequences [32–34]. Here, we present a modified sequence pattern for LRE with two alternating repetition times T_{R1} and T_{R2} for suppressing larger spectral bands referred to as dual-T_R LRE (dT_RLRE) hereafter.

The modified Bloch equation for dT_RLRE reads:

$$\begin{aligned}\frac{d}{dt}M_{xy}(t,\Delta\omega)=[i\Delta\omega-1/T_2]M_{xy}(t,\Delta\omega)+\alpha(t)\sum_{n=0}^{n_{\max}}\delta(t-n(T_{R1}\\ +T_{R2}))M_z(t,\Delta\omega)+\beta(t)\sum_{n=0}^{n_{\max}}\delta(t-n(T_{R1}+T_{R2})\\ -T_{R1})M_z(t,\Delta\omega).\end{aligned} \tag{6}$$

Assuming flip functions $\alpha(t)$ and $\beta(t)$ with periodicity T_S and small flip angles the solution to Eq. (6) is given by:

$$M_{xy}(t,\Delta\omega)\approx\sum_{n=-\infty}^{\infty}D_{\Omega_n}e^{i\Omega_n t}, \tag{7}$$

with

$$D_{\Omega_n}=M_0\left(\sum_{k=-\infty}^{\infty}\tilde{\alpha}_{n-kN}+\sum_{k=-\infty}^{\infty}\tilde{\beta}_{n-kN}e^{-i\frac{2\pi kT_{R1}}{T_{R1}+T_{R2}}}\right)\frac{i/T_2+(\Omega_n-\Delta\omega)}{1/T_2^2+(\Omega_n-\Delta\omega)^2}.$$

The steady-state signal is thus a sum of Lorentzian peaks weighted by a linear combination of the Fourier coefficients $\tilde{\alpha}_k$ and $\tilde{\beta}_k$ of the two flip functions.

In contrast to the coefficients C_Ω with $C_\Omega = C_{\Omega+Nk}$ in standard LRE (Eq. (1)) the coefficients D_{Ω_n} are in general different from $D_{\Omega_{n+Nk}}$. Thereby the transverse magnetization loses its $1/(T_{R1}+T_{R2})$ – periodicity.

We choose the flip functions $\alpha(t)$ and $\beta(t)$ such that their Fourier coefficients are only different from zero within the zero-order frequency band i.e. $\tilde{\alpha}_l = \tilde{\beta}_l = 0$ for $l \notin \{-(N-1)/2, \ldots, (N-1)/2\}$, and again restrict our considerations to flip functions exciting a coherent passband at constant strength:

$$\alpha(t) = \alpha_0 \sum_{j=-m}^{m} \cos(\Omega_j t), \quad \beta(t) = \beta_0 \sum_{l=-m}^{m} cos(\Omega_l t), \qquad m \leqslant (N-1)/2, \quad \alpha_0,\ \beta_0 \in \mathbb{C}. \tag{8}$$

For the amplitude of the Lorentz peaks follows:

$$D_{\Omega_n} = M_0 \left(\tilde{\alpha}_{(n+\frac{N-1}{2} \bmod N)-(N-1)/2} + \tilde{\beta}_{(n+\frac{N-1}{2} \bmod N)-(N-1)/2} e^{-i\frac{2\pi T_{R1}}{T_{R1}+T_{R2}}x} \right) \times \frac{i/T_2 + (\Omega_n - \Delta\omega)}{1/T_2^2 + (\Omega_n - \Delta\omega)^2}. \tag{9}$$

Here, the integer x represents the off-resonance order of the frequency band that contains Ω_n (i.e. $\Omega_n \in \{\Omega_{xN-(N-1)/2}, \ldots, \Omega_{xN+(N-1)/2}\}$). By choosing $\beta_0 = -\alpha_0$ all Fourier coefficients fulfil the relation $\tilde{\beta}_n = -\tilde{\alpha}_n$ and the zero-order frequency band is completely suppressed whereas frequencies within other bands are excited with non-zero amplitude. An example of a flip function design is shown in Fig. 2. An increased stopband width can be achieved by choosing $T_{R1} + T_{R2}$ smaller than $2T_R$ of standard LRE. To keep the sum of the two repetition times short we restricted signal readout to the larger T_{R2}.

In analogy to standard LRE the power deposition of dT_RLRE is given by:

$$w \propto \frac{(2m+1)}{T_{R1}+T_{R2}} \left(|\alpha_0|^2 + |\beta_0|^2 \right). \tag{10}$$

2.1.3. Echo-planar spectroscopic imaging

In EPSI k–t-space is read out by a zigzag readout train after each excitation with Ernst angle α_E (Fig. 1).

The time for phase encoding, prephasing and spoiling is kept as short as possible thereby optimizing SNR_t. Though reducing SNR_t slightly, ramp sampling has been switched off for both LRE and EPSI thereby avoiding gridding problems. The power deposition at repetition time T_{R_EPSI} is given by:

$$w \propto \frac{\alpha_E^2}{T_{R\_EPSI}}. \tag{11}$$

3. Computer simulations

Matrix descriptions of the Bloch equations were implemented in IDL (*Interactive Data Language Version 6.3; Research Systems Inc.*) and numerically solved for steady-state conditions for standard LRE and dT_RLRE. The duration of excitation pulses were assumed to be infinitesimally small for all simulated sequences, a valid assumption for low flip angles and short pulses [37].

For LRE equally sized stop- and passbands were chosen, i.e. $(2m+1) \approx N/2$ in Eqs. (2) and (8). In dT_RLRE we set $|\beta_0| = |\alpha_0|$. Signal amplitudes were optimized by stepwise scaling the flip function and calculating the Ernst angle for EPSI. In EPSI a time gap of 0.6 ms plus 50% of an echo spacing was assumed before data collection. Spectral bandwidths of LRE and EPSI were set identical. Given differences in sampling efficiency in EPSI, LRE and dT_RLRE the readout gradient strengths were adjusted appropriately. Accordingly, noise levels in standard LRE and dT_RLRE were increased relative to EPSI assuming the receiver to be blanked 1.3 ms, 2.3 ms and 0.3 ms between subsequent readout windows in LRE, dT_RLRE and EPSI, respectively. Finally, the ratios SNR_t(LRE)/SNR_t(EPSI) and SNR_t(dT_RLRE)/SNR_t(EPSI) were calculated for different combinations of spectral resolution and spectral bandwidth for on-resonant protons. Furthermore the dependence of these ratios on relaxation times was studied to figure out metabolites delivering high signal as potential targets for LRE spectroscopy.

For the comparison of experimentally and numerically estimated sensitivity ratios measured relaxation constants as well as all time parameters of the implemented sequences were adapted from the phantom experiments. In particular a bandwidth of 1222 Hz was assumed for EPSI and 312.5 Hz in LRE and dT_RLRE. Numerically optimized flip angles were used.

4. Experiments

Standard LRE, dT_RLRE and EPSI were implemented on a 3T Philips Achieva system (Philips Healthcare, Best, The Netherlands). In-vitro experiments were performed in water phantoms doped with $MnCl_2$ (T_1 = 1090 ms; T_2 = 86 ms for SNR_t measurements and T_1 = 950 ms; T_2 = 87 ms for the other experiments) and in phantoms filled with olive oil (T_1 = 260 ms; T_2 = 69 ms).

For the SNR_t measurements a 15 mm slice was excited either in olive oil or water using the same sinc-Gaussian pulse for LRE, dT_RLRE and EPSI. A field of view of $90 \times 90\ mm^2$ was acquired using a 60×60 matrix. Scans at a spectral resolution of 4.8 Hz, 5.7 Hz and 6.7 Hz were acquired for all three sequence types using a bandwidth of 1222 Hz in EPSI and 312.5 Hz in LRE and dT_RLRE. Flip functions exciting 50% of the total bandwidth were used for LRE and dT_RLRE. Signal was optimized for each set of parameters and sequence type by acquiring a series of data sets with different flip angles. Scan efficiency was 60% in EPSI and 34–36% in dT_RLRE. Due to B_1 constraints scan efficiency was lowered in all LRE protocols requiring a larger maximum flip angle in the flip function. At a resolution of 4.8 Hz the maximum angle in the flip function for optimum signal in oil was 46.2° resulting in an efficiency of 53% whereas efficiency was 61% for the water scan at 6.7 Hz requiring a maximum flip angle of 25.3° only. The experimental parameters were used in the simulation programs.

Noise data were recorded by switching off gradients in zero flip angle scans.

Excitation functions were visualized in phantoms by applying a constant shim gradient of 0.35 mT/m in-plane (T_R = 4.8 ms; T_S = 955 ms in LRE and dT_RLRE scan; T_S = 1042 ms in the dT_RLRE scan with an additional CHESS module of 72 ms duration).

In dT_RLRE a module for additional water suppression was introduced. For this purpose a set of consecutive pulses with very small flip angle was skipped in both flip functions $\alpha(t)$ and $\beta(t)$ along with data sampling to accommodate 86.4 ms for a 650 Hz CHESS sequence.

For the ex vivo experiments a sample of human carotid atherosclerotic plaque was frozen with liquid nitrogen immediately after endarterectomy and kept at −80 °C. For the MR experiments the specimen was defrosted and mechanically fixed in a bottle with demineralised water. The sample was slowly heated to 42 °C in a water bath to melt crystallized cholesterol esters.

Three-dimensional spectroscopic imaging of the plaque sample was performed at 37.0 °C (±0.4 °C) with the dT_RLRE and the EPSI acquisition scheme both with CHESS water suppression. Sequence parameters were as follows: FOV: $95 \times 95 \times 37\ mm^3$; matrix size: $48 \times 83 \times 32$ resulting in a spatial resolution of 1.95×1.15

$\times$ 1.15 mm^3; keeping the frequency encoded readout duration short, the measurement direction was placed along the cylinder axis of the plaque resulting in an isotropic resolution for cross sections with a slice thickness of 1.95 mm; spectral resolution: 6.2 Hz; duration of the frequency encoded spectral readout train: 160.8 ms; excitation centered at −450 Hz relative to the water peak; second order pencil beam shim. The specific parameters for dT_RLRE were: spectral bandwidth: 417 Hz; maximum angle in flip function: 15.8°; T_{R1} = 0.6 ms; T_{R2} = 1.8 ms; T_S: 247 ms (including 86.4 ms for water suppression); passband width: 206 Hz. For the EPSI scan the bandwidth was 1432 Hz; T_R: 257 ms (not including 88 ms for water suppression); flip angle: 70°. Data were acquired with an elliptical *k*-space shutter within one average in a scan time of 7 min for dT_RLRE and 9 min for EPSI, respectively. The longer measurement time in 3D EPSI is a result of duty cycle restrictions prolonging T_R. For comparison a single volume (15 $\times$ 15 $\times$ 36 mm^3) STEAM spectrum was measured with a spectral resolution of 3.52 Hz; T_R/T_E: 1100 ms/9 ms; CHESS water suppression. For imaging structural information multi-slice spin echo sequences with T_1, T_2 and proton-density weighting were acquired with an in-plane resolution of 0.25 $\times$ 0.25 mm^2 and a slice thickness of 1 mm. Lipids were stained with Oil Red O staining in histological sections.

Table 1
Numerically estimated fluctuations of the spectral peak amplitudes within the passband. Smoothness is lost at combinations of long T_2^* and poor spectral resolution.

$\Delta f\, T_2^*$	T_2^* at Δf = 2.5 Hz	Max. passband ripple in %
0.015	6	0.11
0.03	12	0.44
0.0625	25	1.87
0.125	50	6.85
0.1875	75	12.99
0.25	100	18.41
0.375	150	26.20

5. Results

Excitation functions as simulated for standard LRE and dT_RLRE are shown in Fig. 2. The inset magnifies passband ripples, which arise from truncation. The flank of the individual passband can be approximated by the downslope of a Lorentz peak and may prevent complete signal suppression in the stopbands. For dT_RLRE the intensity of the individual passband varies as does the width of the stopbands. In Table 1 the dependency of passband ripple on T_2^* and spectral resolution is given. The ratios are defined as difference between passband maximum and adjacent local minimum relative to the maximum. The values show that the smoothness of the excitation profiles is lost for combinations of long T_2^* and poor spectral resolution (large Δf). The evolution of the steady-state signal on- and off-resonant is demonstrated in Fig. 3a and b, respectively. The comparison with the intensity-scaled FID shows that LRE excitation recovers spectral frequencies accurately and hence demonstrates feasibility of LRE for recording spectra.

The results of the simulation were verified in experiments using a cylindrical water phantom (Fig. 4). The excitation functions in phantoms (gray inserts) are in good agreement with the results from numerical calculations. The degree of suppression is found to be significantly increased in the broad stopband in dT_RLRE (Fig. 4b) as compared to conventional LRE (Fig. 4a). Modifying the dT_RLRE sequence with an additional water suppression module (Fig. 4c) allows specific excitation of a narrow spectral domain, e.g. of the range of aliphatic lipid signals.

Fig. 5 represents passband amplitudes and power deposition values for LRE and dT_RLRE as a function of the maximum angle in the flip function. Experimental data (symbols with error bars)

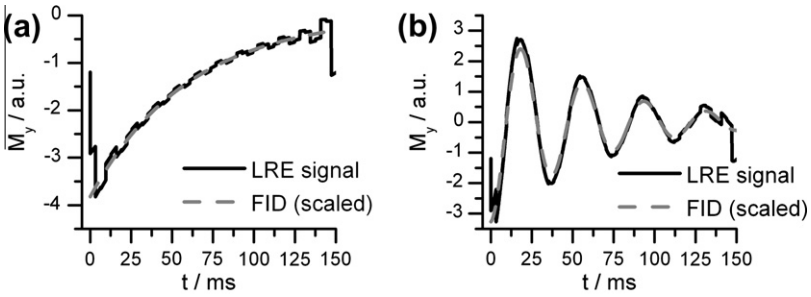

Fig. 3. The numerically derived time course of steady-state LRE signal within one period of the flip function is shown for on-resonant protons (a) and an off-resonance frequency of 26.6 Hz (b). The comparison with free induction decay (dashed gray curves) demonstrates the feasibility of LRE for spectroscopy (T_R = 3.2 ms; T_S = 150.4 ms; T_E = 1 ms; T_1 = 280 ms; T_2^* = 60 ms; flip function: N = 47; (2 m + 1) = 23; α_0 = 0.5°).

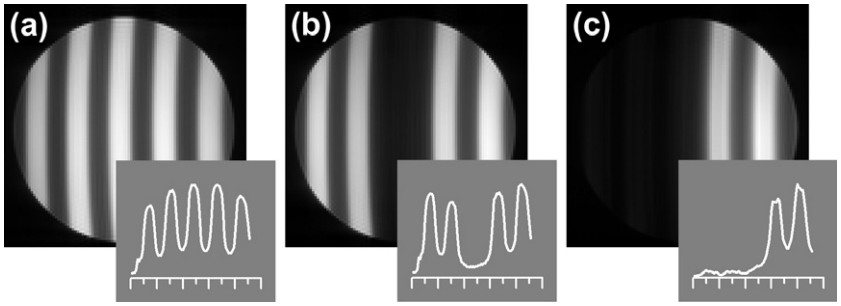

Fig. 4. Visualization of the excitation function of standard LRE (T_R = 4.8 ms; T_S = 955.2 ms; α_0 = 0.2°) (a) dT_RLRE (T_{R1} = 1.2 ms; T_{R2} = 3.6 ms; T_S = 955.2 ms; α_0 = β_0 = 0.1°) (b) and dT_RLRE with an additional water suppression module (T_{R1} = 1.2 ms; T_{R2} = 3.6 ms; T_S = 1041.6 ms; α_0 = β_0 = 0.1°; CHESS: duration: 72 ms; suppression band: 1 kHz). During the scan a constant gradient (0.35 mT/m) has been applied in read direction to spatially resolve the excitation pattern. Total spectral area and profiles along a center line as insets are shown. Equally sized stop- and passbands were chosen for LRE. The broad stopband in dT_RLRE is approximately three times wider than a normal stopband.

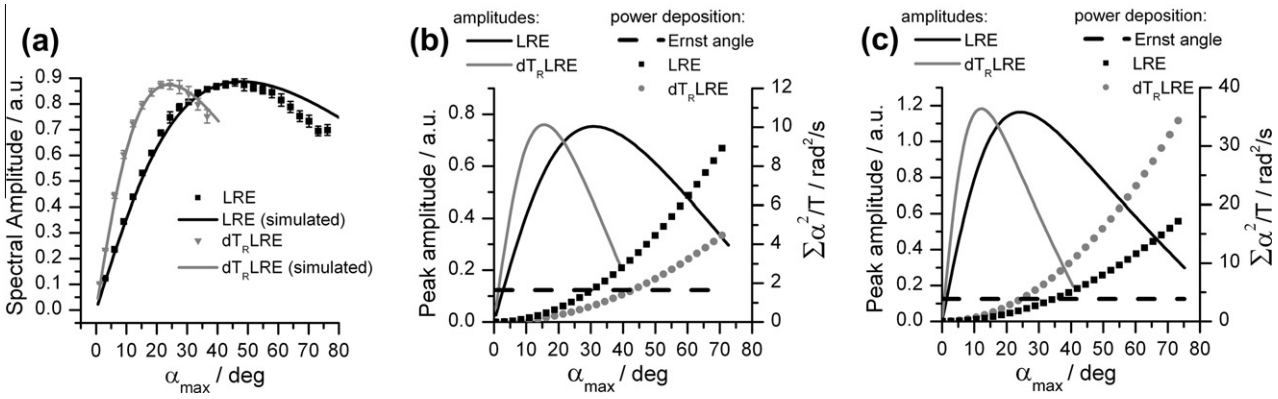

Fig. 5. (a) Peak amplitudes in the spectral domain (real part) plotted as a function of the maximum angle in the flip function $\alpha(t)$ for LRE and dT_RLRE. Simulated (lines) and measured values (symbols) match well for small flip angles. Parameters: T_1 = 950 ms; T_2 = 87 ms; $T_R = T_{R1} + T_{R2}$ = 5.6 ms; T_S = 677.6 ms; N = 121; $(2m + 1)$ = 61. (b and c) Simulated peak amplitudes in the spectral domain are plotted as a function of the maximum angle in the flip function $\alpha(t)$ for LRE and dT_RLRE (straight curves; left vertical axis). In the same diagrams the average quadratic flip angle per unit time is presented as a measure for the power deposition (symbols; right vertical axis). (b) T_1 = 950 ms; T_2 = 87 ms; $T_R = T_{R1} + T_{R2}$ = 5.6 ms; T_S = 677.6 ms; N = 121; $(2m + 1)$ = 61. (c) T_1 = 450 ms; T_2 = 50 ms; $T_R = T_{R1} + T_{R2}$ = 5.6 ms; T_S = 196 ms; N = 35; $(2m + 1)$ = 17. For both parameter sets the power deposition for the LRE sequences at the angle providing maximum signal is significantly smaller compared to an excitation with the Ernst angle (dashed horizontal line) assuming the same pulse shape and bandwidth.

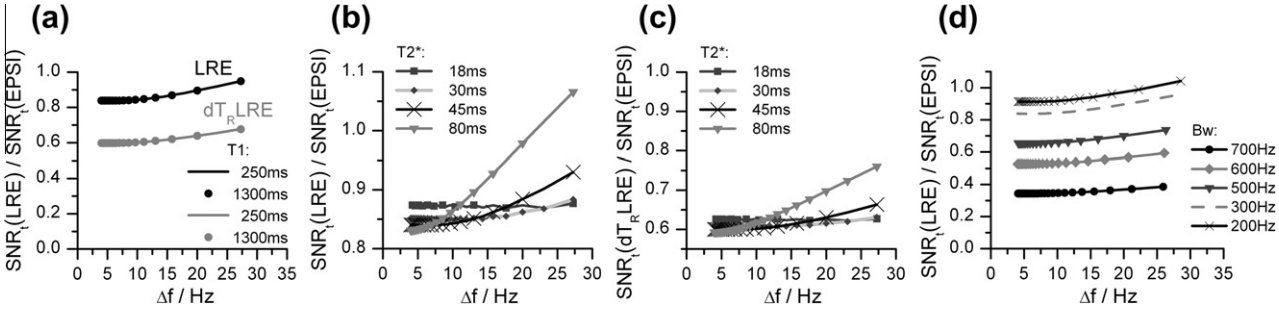

Fig. 6. Dependence of the simulated sensitivity ratios SNR_t(LRE)/SNR_t(EPSI) and SNR_t(dT_RLRE)/SNR_t(EPSI) on T_1, T_2^* and spectral bandwidth. Using optimal flip angles, the influence of the longitudinal relaxation rate is marginal (a). LRE and dT_RLRE perform better at small bandwidth (d) low spectral resolution and long transverse relaxation time (b and c). Parameters: BW: 300 Hz; T_2^*: 50 ms (a); BW: 300 Hz; T_1:750 ms (b and c); T_1: 500 ms; T_2^*: 50 ms (d).

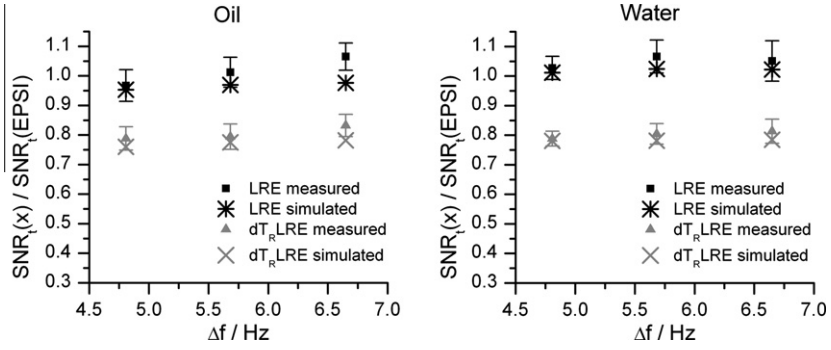

Fig. 7. Measured and simulated SNR_t values for LRE, dT_RLRE relative to the SNR_t of EPSI in olive oil (left) and doped water (right diagram).

and simulation results (lines), weighted by the excitation profile of a sinc-Gaussian pulse, agree well for small flip angles but do differ slightly for larger peak amplitudes (Fig. 5a). For both LRE and dT_RLRE the power deposition at the position of maximum signal is remarkably smaller relative to Ernst angle excitation applying the same RF-waveforms, which is indicated by a dashed horizontal line in Fig. 5b and c.

Fig. 6 compares SNR_t(LRE)/SNR_t(EPSI) and SNR_t(dT_RLRE)/SNR_t(EPSI) based on simulations. The two ratios are only weakly depend on T_1 (Fig. 6a), but increase with increasing T_2^* (Fig. 6b and c). The influence of the spectral bandwidth on the sensitivity ratios is illustrated in Fig. 6d. As long as the total number of sampling points is kept constant the SNR_t of an EPSI sequence without ramp sampling does only slightly depend on spectral bandwidth [6]. In contrast LRE benefits from increased sampling efficiency at low spectral bandwidth. LRE and dT_RLRE yield inferior SNR_t values to EPSI.

Fig. 7 depicts SNR_t measured experimentally for EPSI (spectral bw: 1222 Hz), LRE and dT_RLRE (spectral bw: 312.5 Hz) in water and oil phantoms for different spectral resolutions as well as simulated values for the respective experimental parameters. Conventional LRE yields higher SNR_t values than dT_RLRE. The pair of

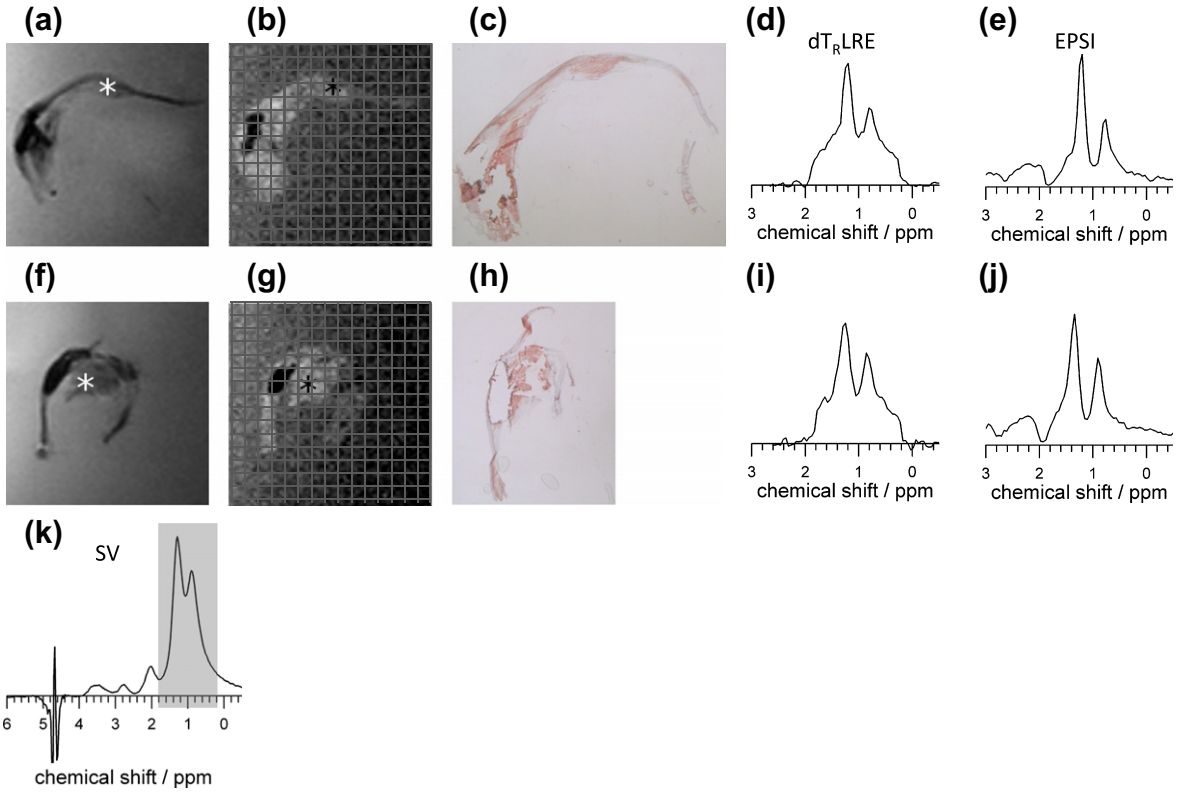

Fig. 8. T_2 weighted spin echo (a and f); T_1 weighted spin echo (b and g); and histological sections (c and h) of an atherosclerotic carotid plaque ex vivo. Panels (d and i) show the real part of dT_RLRE-spectra and panels (e and j) display EPSI-spectra collected from a $1.95 \times 1.15 \times 1.15$ mm^3 voxel marked with an asterisk in the anatomical images (spectra with moderate exponential filter). The grid in the T_1 weighted images corresponds to the in-plane resolution of the spectroscopic imaging sequences. The passbands of the dT_RLRE-spectra are in accordance with the gray shaded part of the single voxel STEAM spectrum covering the entire plaque (k). Local differences in lipid composition are evident comparing the spectra from the two selected voxels.

bandwidths has been chosen with regard to capable values for lipid spectroscopy. Measured and computed sensitivities for LRE are slightly higher whereas those of dT_RLRE are lower compared to EPSI.

Finally the performance of the LRE sequences and EPSI have been evaluated by studying arteriosclerotic plaques ex vivo. Anatomical images with either T_2 or T_1 weighting of two sections are depicted in Fig. 8a, b and f, g respectively. dT_RLRE and EPSI spectra from voxels indicated in the anatomical images (asterisk) are shown in Figs. 8d, i and e, j. Red staining in the images of histological sections (Fig. 8c and h) indicates lipid rich regions at these positions. Methyl (0.8 ppm) and methylene peaks (1.2 ppm) are clearly distinguishable. EPSI and dT_RLRE spectra match well though dT_RLRE is characterized by a clear cut between stopband and passband and an underlying broad signal that extends across the width of the passband. The Comparison of spectra 8d, 8e with 8i, 8j reveal that the chemical composition of the plaque is heterogeneous, i.e. the ratio of the methylene and methyl signal intensity depends on the location. For comparison a single voxels STEAM spectrum of the whole plaque is shown (Fig. 8k). The region shaded in gray in the single voxel spectrum corresponds to the primary passband excited in the dT_RLRE sequence. Signals occurring at chemical shift values above 2 ppm, in particular that of water protons are suppressed by a combination of sequence intrinsic stopbands and periodically repeated water suppression pulses.

6. Discussion

In this work, the sensitivity and power deposition of LRE spectroscopic imaging were compared to EPSI using computer simulations and phantom experiments for a range of relaxation times and spectral resolutions. A modified LRE scheme employing alternating repetition times has been proposed to accommodate sufficient spectral bandwidth without aliasing for spectroscopic imaging at a clinical 3 T system. It has furthermore been shown that very low excitation angles in the flip function of the modified dT_RLRE scheme may be skipped to include additional water suppression pulses. This modified dT_RLRE sequence was used to map cholesterol content in arteriosclerotic ex vivo plaques to demonstrate the feasibility of the approach.

Our simulations show that the ratios SNR_t(LRE)/SNR_t(EPSI) and SNR_t(dT_RLRE)/SNR_t(EPSI) only marginally depend on T_1, provided flip angles were adjusted accordingly.

Overall the sensitivity of EPSI was found to be higher compared to LRE. This primarily relates to the higher sampling efficiency and thus lower noise level of EPSI which allows for continuous sampling after excitation while in LRE data acquisition is interrupted by RF-pulses. The increased noise in LRE and dT_RLRE outweighs the gain in signal relative to EPSI. LRE was found to outperform EPSI with respect to sensitivity only at low spectral resolution and T_2^* values above 80 ms corresponding to a spectral line width of $\approx$4 Hz which is an unrealistic value for most metabolites in vivo at 3 T. In addition it has to be considered that a smooth passband in LRE is only generated for small products $\Delta f\, T_2^*$.

The sensitivity values measured in phantom experiments revealed a comparable SNR_t performance of LRE and EPSI and a lower sensitivity of dT_RLRE due to lower sampling efficiency. Experimental results and simulations were found to agree well. The SNR_t values were collected at fourfold higher bandwidth for EPSI relative to LRE and dT_RLRE. Thus, the sensitivity of EPSI was slightly decreased since ramp sampling was switched off for all sequences.

Taking the average quadratic flip angle per time as a measure for the power deposition a lower specific absorption rate was found for LRE and dT_RLRE compared to EPSI. SAR could be reduced in EPSI by applying longer RF-pulses which is difficult in LRE-type sequences due to the need for short repetition times. Applying longer excitation pulses will on the other hand result in a lower pulse bandwidth and therefore in a higher separation between excited slices due to off-resonance effects. This can be an issue in 2D acquisitions and at low field homogeneity. In addition increasing pulse durations will slightly increase the echo time which results in a signal loss of metabolites with very short T_2^* values.

For medical applications the sequence intrinsic suppression might be insufficient to prevent aliasing and additional water suppression modules have to be introduced into the sequence lowering acquisition efficiency. The detection of lipid signal constitutes a favorable situation for a method such as LRE spectroscopy: given the high signal within a limited spectral range lipid spectroscopy may profit from rapid steady-state sequence since only a few averages will be necessary. The spectral resolution in dT_RLRE is less limited than in multi-echo based methods such as IDEAL [38–40]. We therefore tested the dT_RLRE sequence with additional water suppression in a human atherosclerotic plaque embedded in water.

Methyl and methylene peaks have different ratios depending on the position in the atheroma suggesting local variations of lipid composition in the plaque. Providing an average of all lipid rich regions this information cannot be derived from the single voxel spectrum. As lipid depositions are considered to be a crucial parameter for plaque stability [19] the information about local differences in the composition of lipids can potentially be of clinical importance and can help classifying the risk of an atherosclerotic plaque. Additionally, spatially resolved in vivo MR-spectroscopy of cholesteryl esters could be a promising tool to study the effects of cholesterol lowering drugs non-invasively or to gain further insight into the progression of atherosclerotic disease. To this end, our ex vivo study indicates the potential of dT_RLRE and EPSI for plaque spectroscopy with low SAR.

By increasing T_R the ratio of data acquisition to periods with blanked receiver can be expanded. As spectral bandwidth is thereby lowered, this might be an option to increase SNR_t for applications containing spectral information within a small region of interest only or at low field systems. Also stronger gradient power will increase sampling efficiency making animal systems an interesting platform for LRE. It also remains to be investigated by how much the number of pulses in LRE can be reduced while conserving the excitation function with stopbands for intrinsic water suppression.

In summary, both dT_RLRE and EPSI permit spectroscopy of lipid compounds with high spatial resolution within short scan times. The limited sampling efficiency of LRE/dT_RLRE, however, offsets the gains in signal and hence results in lower SNR_t compared to EPSI. In contrast, power deposition in LRE sequences is lower compared to EPSI and renders LRE an alternative in cases were SAR is a concern.

Acknowledgments

The authors wish to thank Christine Lohmann for her contribution to this work by preparing the histological sections of plaque specimens. It was a great help for us. Many thanks to Dr. Zoran Rancic and Prof. Dr. Philipp A. Kaufmann for their contribution to the work by supplying us with carotid plaques.

We also thank the Zurich Center for *Integrative Human Physiology* (ZIHP) for financial support.

Appendix A

A.1. The power deposition for a flip function of the type given in formula (2) is

$$\begin{aligned} w \propto \frac{1}{T_S}\sum_{k=0}^{N-1}|\alpha_k|^2 &= \frac{|\alpha_0|^2}{T_S}\sum_{k=0}^{N-1}\left(\mathrm{Re}\left(\sum_{j=-m}^{m}\exp\left(i2\pi kj/N+i\varphi_j\right)\right)\right. \\ &\quad \left.\times\,\mathrm{Re}\left(\sum_{l=-m}^{m}\exp\left(i2\pi kl/N+i\varphi_l\right)\right)\right) \\ &= \frac{|\alpha_0|^2}{2T_S}\mathrm{Re}\left(\sum_{k=0}^{N-1}\sum_{j=-m}^{m}\sum_{l=-m}^{m}\left(\exp\left(i2\pi k(j+l)/N\right.\right.\right. \\ &\quad \left.\left.\left.+i\left(\varphi_j+\varphi_l\right)\right)+\exp\left(i2\pi k(j-l)/N+i\left(\varphi_j-\varphi_l\right)\right)\right)\right) \\ &= \frac{|\alpha_0|^2}{2T_S}\mathrm{Re}\left(\sum_{j=-m}^{m}\sum_{l=-m}^{m}N\left(\exp\left(i\left(\varphi_j+\varphi_l\right)\right)\delta_{j,-l}\right.\right. \\ &\quad \left.\left.+\exp\left(i\left(\varphi_j-\varphi_l\right)\right)\delta_{j,l}\right)\right) \\ &= \frac{|\alpha_0|^2}{T_S}N(2m+1) = \frac{|\alpha_0|^2}{T_R}(2m+1). \end{aligned}$$

In the third and fourth line we used the respectively relations

$$\mathrm{Re}(a)\mathrm{Re}(b) = \frac{1}{2}\mathrm{Re}(ab+ab^*) \text{ and } \sum_{k=0}^{N-1}x^k = \begin{cases} N \text{ for } x=1 \\ \frac{x^N-1}{x-1} \text{ else} \end{cases}.$$

A.2. Formal solution of the Bloch equations for the transverse magnetization M_{xy}

$$\begin{aligned} \frac{d}{dt}M_{xy}(t,\Delta\omega) &= [i\Delta\omega - 1/T_2]M_{xy}(t,\Delta\omega)+\alpha(t) \\ &\quad \times\sum_{n=0}^{n_{\max}}\delta(t-n\cdot T_R)M_z(t,\Delta\omega). \end{aligned}$$

at the echo time T_E after a set of k RF-pulses with amplitudes $\alpha(t)$ applied every T_R:

$$\begin{aligned} M_{xy}(kT_R+T_E,\Delta\omega) &= e^{(kT_R+T_E)(-\frac{1}{T_2}+i\Delta\omega)}\sum_{n=0}^{k}\alpha(nT_R)M_z(nT_R)e^{nT_R(\frac{1}{T_2}-i\Delta\omega)} \\ &= M_{xy}(kT_R+T_E,\Delta\omega+2\pi/T_R). \end{aligned}$$

References

[1] T.R. Brown, B.M. Kincaid, K. Ugurbil, NMR chemical-shift imaging in 3 dimensions, in: Proceedings of the National Academy of Sciences of the United States of America-Biological Sciences, vol. 79, 1982, pp. 3523–3526.
[2] U. Dydak, M. Weiger, K.P. Pruessmann, D. Meier, P. Boesiger, Sensitivity-encoded spectroscopic imaging, Magn. Reson. Med. 46 (2001) 713–722.
[3] A.A. Maudsley, G.B. Matson, J.W. Hugg, M.W. Weiner, Reduced phase-encoding in spectroscopic imaging, Magn. Reson. Med. 31 (1994) 645–651.
[4] E. Adalsteinsson, P. Irarrazabal, S. Topp, C. Meyer, A. Macovski, D.M. Spielman, Volumetric spectroscopic imaging with spiral-based *k*-space trajectories, Magn. Reson. Med. 39 (1998) 889–898.
[5] C.V. Schirda, C. Tanase, F.E. Boada, Rosette spectroscopic imaging: optimal parameters for alias-free, high sensitivity spectroscopic imaging, J. Magn. Reson. Imaging 29 (2009) 1375–1385.
[6] R. Pohmann, M. von Kienlin, A. Haase, Theoretical evaluation and comparison of fast chemical shift imaging methods, J. Magn. Reson. 129 (1997) 145–160.
[7] W. Dreher, C. Geppert, M. Althaus, D. Leibfritz, Fast proton spectroscopic imaging using steady-state free precession methods, Magn. Reson. Med. 50 (2003) 453–460.
[8] C. Schuster, W. Dreher, C. Geppert, D. Leibfritz, Fast 3D H-1 spectroscopic imaging at 3 tesla using spectroscopic missing-pulse SSFP with 3D spatial preselection, Magn. Reson. Med. 57 (2007) 82–89.

[9] O. Speck, K. Scheffler, J. Hennig, Fast P-31 chemical shift imaging using SSFP methods, Magn. Reson. Med. 48 (2002) 633–639.
[10] K. Scheffler, S. Lehnhardt, Principles and applications of balanced SSFP techniques, Eur. Radiol. 13 (2003) 2409–2418.
[11] K.W. Eberhardt, M. Schar, C. Barmet, J. Tsao, P. Boesiger, S. Kozerke, Linear response equilibrium, J. Magn. Reson. 178 (2006) 142–154.
[12] P. Mansfield, Spatial-mapping of the chemical-shift in NMR, Magn. Reson. Med. 1 (1984) 370–386.
[13] S. Posse, C. Decarli, D. Lebihan, 3-Dimensional echo-planar MR spectroscopic imaging at short echo times in the human brain, Radiology 192 (1994) 733–738.
[14] W.L. Du, Y.P.P. Du, U. Bick, X.B. Fan, P.M. MacEneaney, M.A. Zamora, M. Medved, G.S. Karczmar, Breast MR imaging with high spectral and spatial resolutions: preliminary experience, Radiology 224 (2002) 577–585.
[15] T. Wilhelm, P. Bachert, In vivo P-31 echo-planar spectroscopic imaging of human calf muscle, J. Magn. Reson. 149 (2001) 126–130.
[16] S. Foxley, X.B. Fan, D. Mustafi, C. Haney, M. Zamora, E. Markiewicz, M. Medved, A.M. Wood, G.S. Karczmar, Sensitivity to tumor microvasculature without contrast agents in high spectral and spatial resolution MR images, Magn. Reson. Med. 61 (2009) 291–298.
[17] W.L. Du, X.B. Fan, S. Foxley, M. Zamora, J.N. River, R.M. Culp, G.S. Karczmar, Comparison of high-resolution echo-planar spectroscopic imaging with conventional MR imaging of prostate tumors in mice, NMR Biomed. 18 (2005) 285–292.
[18] S. Foxey, X.B. Fan, S.A. Jansen, M. Zamora, E. Markiewicz, H. Al-Ahmadie, G.S. Karczmar, High spectral and spatial resolution MRI of age-related changes in murine prostate, Magn. Reson. Med. 60 (2008) 575–581.
[19] M.J. Davies, P.D. Richardson, N. Woolf, D.R. Katz, J. Mann, Risk of thrombosis in human atherosclerotic plaques – role of extracellular lipid, macrophage and smooth-muscle cell content, Br. Heart J. 69 (1993) 377–381.
[20] M. Shinnar, J.T. Fallon, S. Wehrli, M. Levin, D. Dalmacy, Z.A. Fayad, J.J. Badimon, M. Harrington, E. Harrington, V. Fuster, The diagnostic accuracy of ex vivo MRI for human atherosclerotic plaque characterization, Arteriosclerosis Thrombosis Vascular Biol. 19 (1999) 2756–2761.
[21] B.D. Coombs, J.H. Rapp, P.C. Ursell, L.M. Reilly, D. Saloner, Structure of plaque at carotid bifurcation – high-resolution MRI with histological correlation, Stroke 32 (2001) 2516–2521.
[22] R.R. Ronen, S.E. Clarke, R.R. Hammond, B.K. Rutt, Carotid plaque classification: defining the certainty with which plaque components can be differentiated, Magn. Reson. Med. 57 (2007) 874–880.
[23] C.H. Maynor, H.C. Charles, R.J. Herfkens, S.A. Suddarth, G.A. Johnson, Chemical-shift imaging of atherosclerosis at 7.0-Tesla, Invest. Radiol. 24 (1989) 52–60.
[24] J. Zajicek, J.D. Pearlman, M.B. Merickel, C.R. Ayers, J.R. Brookeman, M.F. Brown, High-resolution proton NMR-spectra of human arterial plaque, Biochem. Biophys. Res. Commun. 149 (1987) 437–442.
[25] J.D. Pearlman, J. Zajicek, M.B. Merickel, C.S. Carman, C.R. Ayers, J.R. Brookeman, M.F. Brown, High-resolution H-1-NMR spectral signature from human atheroma, Magn. Reson. Med. 7 (1988) 262–279.
[26] D.M. Small, Duff George, Lyman memorial lecture – progression and regression of atherosclerotic lesions – insights from lipid physical biochemistry, Arteriosclerosis 8 (1988) 103–129.
[27] F.L. Ruberg, J. Viereck, A. Phinikaridou, Y. Qiao, J. Loscalzo, J.A. Hamilton, Identification of cholesteryl esters in human carotid atherosclerosis by ex vivo image-guided proton MRS, J. Lipid Res. 47 (2006) 310–317.
[28] G.E. Gold, J.M. Pauly, G.H. Glover, J.C. Moretto, A. Macovski, R.J. Herfkens, Characterization of atherosclerosis with a 1.5-T imaging-system, JMRI – J. Magn. Reson. Imaging 3 (1993) 399–407.
[29] W.R. Overall, D.G. Nishimura, B.S. Hu, Steady-state sequence synthesis and its application to efficient fat-suppressed imaging, Magn. Reson. Med. 50 (2003) 550–559.
[30] M. Schar, S. Kozerke, S.E. Fischer, P. Boesiger, Cardiac SSFP imaging at 3 tesla, Magn. Reson. Med. 51 (2004) 799–806.
[31] T. Cukur, D.G. Nishimura, Fat-water separation with alternating repetition time balanced SSFP, Magn. Reson. Med. 60 (2008) 479–484.
[32] T. Cukur, D.G. Nishimura, Multiple repetition time balanced steady-state free precession imaging, Magn. Reson. Med. 62 (2009) 193–204.
[33] J. Leupold, J. Hennig, K. Scheffler, Alternating repetition time balanced steady state free precession, Magn. Reson. Med. 55 (2006) 557–565.
[34] K.S. Nayak, H.L. Lee, B.A. Hargreaves, B.S. Hu, Wideband SSFP: alternating repetition time balanced steady state free precession with increased band spacing, Magn. Reson. Med. 58 (2007) 931–938.
[35] S.S. Vasanawala, J.M. Pauly, D.G. Nishimura, Fluctuating equilibrium MRI, Magn. Reson. Med. 42 (1999) 876–883.
[36] J. Absil, V. Denolin, T. Metens, Fat attenuation using a dual steady-state balanced-SSFP sequence with periodically variable flip angles, Magn. Reson. Med. 55 (2006) 343–351.
[37] O. Bieri, K. Scheffler, SSFP signal with finite RF pulses, Magn. Reson. Med. 62 (2009) 1232–1241.
[38] G.H. Glover, E. Schneider, 3-Point Dixon technique for true water fat decomposition with B0 inhomogeneity correction, Magn. Reson. Med. 18 (1991) 371–383.
[39] J. Leupold, O. Wieben, S. Mansson, O. Speck, K. Scheffler, J.S. Petersson, J. Hennig, Fast chemical shift mapping with multiecho balanced SSFP, Magn. Reson. Mater. Phys. Biol. Med. 19 (2006) 267–273.
[40] S.B. Reeder, A.R. Pineda, Z.F. Wen, A. Shimakawa, H.Z. Yu, J.H. Brittain, G.E. Gold, C.H. Beaulieu, N.J. Pelc, Iterative decomposition of water and fat with echo asymmetry and least-squares estimation (IDEAL): application with fast spin-echo imaging, Magn. Reson. Med. 54 (2005) 636–644.